



Compressive response and microstructural evolution of in-situ TiB₂ particle-reinforced 7075 aluminum matrix composite

Han WANG, Hai-ming ZHANG, Zhen-shan CUI, Zhe CHEN, Dong CHEN

School of Materials Science and Engineering, Shanghai Jiao Tong University, Shanghai 200240, China

Received 6 June 2020; accepted 30 December 2020

Abstract: The hot forming behavior, failure mechanism, and microstructure evolution of in-situ TiB₂ particle-reinforced 7075 aluminum matrix composite were investigated by isothermal compression test under different deformation conditions of deformation temperatures of 300–450 °C and strain rates of 0.001–1 s⁻¹. The results demonstrate that the failure behavior of the composite exhibits both particle fracture and interface debonding at low temperature and high strain rate, and dimple rupture of the matrix at high temperature and low strain rate. Full dynamic recrystallization, which improves the composite formability, occurs under conditions of high temperature (450 °C) and low strain rate (0.001 s⁻¹); the grain size of the matrix after hot compression was significantly smaller than that of traditional 7075Al and ex-situ particle reinforced 7075Al matrix composite. Based on the flow stress curves, a constitutive model describing the relationship of the flow stress, true strain, strain rate and temperature was proposed. Furthermore, the processing maps based on both the dynamic material modeling (DMM) and modified DMM (MDMM) were established to analyze flow instability domain of the composite and optimize hot forming processing parameters. The optimum processing domain was determined at temperatures of 425–450 °C and strain rates of 0.001–0.01 s⁻¹, in which the fine grain microstructure can be gained and particle crack and interface debonding can be avoided.

Key words: in-situ TiB₂ particles; aluminum matrix composite; hot compression deformation; particle fracture; interface debonding; dynamic recrystallization

1 Introduction

Due to the excellent combination of aluminum matrix which has good ductility and toughness and ceramic particles which have high strength and stiffness, the particle reinforced Al matrix composites (PR-AIMCs) have great potential to be applied as light mass materials because of their superior mechanical and physical properties such as high specific strength and stiffness, wear resistance, fatigue resistance, and low thermal expansion coefficient [1,2]. In particular, in-situ PR-AIMCs are increasingly popular due to the evenly distributed particles and better cohesive interfaces between the particles and the matrix [3,4]. However,

the distinct difference in mechanical properties between the metal matrix and the reinforced particles renders the composite rather complicated in plasticity behavior and failure mechanism [5,6]. Therefore, fabricating high-performance PR-AIMC components via metal forming operations requires a full understanding of the plasticity behaviors, microstructure evolution, and failure mechanisms of the composite under specific process condition.

Attempts have been devoted to explore the hot deformation characteristics of PR-AIMCs and to develop constitutive models [7–9]. CHEN et al [10] found that the flow behavior of the SiC/8009Al composite was attributed to the intense dynamic recovery caused by the fine Al₁₂(Fe,V)₃Si-phase dispersoids with a high volume fraction.

GANGOLU et al [11] and SARAVANAN and SENTHILVELAN [12] found that the reinforced particles could increase the average activation energy of the B₄C/A356 and the Al₂O₃/AA7075 composites. PATEL et al [13] found that the softening mechanism of the SiC_p/2014Al composites is caused by two reasons: the interface debonding when Zener–Hollomon parameter (Z) is large, and dynamic recovery/recrystallization (DRX) when Z -parameter is small. Both microstructure evolution and fracture mechanism of PR-ALMCs in hot forming processes are also research hotspots. Some researchers stated that the failure mode of PR-ALMCs is mainly attributed to particle fracture, interface debonding and dimple rupture of the matrix [5,14,15]. LI et al [16] investigated the hot deformation behaviors of a B₄C/6061Al composite; they found that interface debonding and particle crack are more prone to occur under the deformation condition of high strain rate and low temperature, while the adiabatic shear band is more likely observed at a very high strain rate.

Theoretical approaches, for example, the processing map (PM), are increasingly used to optimize the hot forming processing parameters of PR-ALMCs and to explain the microstructure evolution associated with different temperatures and strain rates [17–19]. RAMANATHAN et al [20] constructed the processing map of a SiC/2124Al composite and found that DRX occurred when the maximum power dissipation efficiency (PDE) was up to 38%. By developing PMs at different strain levels, SENTHILKUMAR et al [21] established the relationship between microstructure evolution and process parameters such as temperature, strain rate, and strain for a TiC/5083Al composite, where DRX mainly occurred under conditions of high temperatures (400–450 °C) and low strain rates (0.01–0.08 s⁻¹), while flow localization occurred at high strain rates. In a study of the deformation behavior of SiC_p/2024Al prepared by powder metallurgy, SHAO et al [22] found that finer SiC_p and smaller 2024Al powders can shift the DRX domain to higher strain rates and lower temperatures, and decrease the peak value of PDE. The research of XU et al [23] on a SiC_w/6061Al composite shows that the instability regions predicted by the Prasad's and the Murty's instability criteria are smaller than the actual one,

and the Gegel's instability criterion is not appropriate for the composite.

However, for in-situ PR-ALMCs in which the reinforcing particles are generated by chemical reaction, a full understanding of their unique microstructure, mechanical properties, deformation behaviors, and failure mechanism is still lacking. In this work, the deformation behavior and failure mechanism of an in-situ 6 wt.% TiB₂ PR-ALMCs were investigated by isothermal compression tests at various temperatures from 300 to 450 °C and strain rates from 0.001 to 1 s⁻¹. The microstructure evolution and micro-fractography were examined in detail, and PMs with different instability criteria were specially established for optimizing the hot forming parameters, and microstructure observation was employed to verify the PMs.

2 Experimental

The studied in-situ TiB₂/7075Al composite was synthesized by casting with a mixed salt route. More details about the material preparation process can be found in the work of CHEN et al [24]. A hot extrusion process with an extrusion ratio of 10:1 was employed to fabricate the as-cast material into rods, and the extruded rods were then subjected to the stress-relief annealing at 450 °C for 1 h. The cylindrical hot compression specimens with 10 mm in diameter and 15 mm in height were machined from the rods via wire electrical discharge machining. The height direction of the specimens, i.e., the compressive direction, is parallel to the extrusion direction (ED). Isothermal compression tests were performed on a Gleeble 3500 thermal–mechanical simulator. The process conditions were the combination of temperatures of 300, 350, 400 and 450 °C with strain rates of 0.001, 0.01, 0.1 and 1 s⁻¹. All the specimens were finely polished to minimize the machining defects, and the specimen–anvil interface was lubricated with graphite. The specimens were heated to the designed deformation temperatures at a speed of 5 °C/s, held for 15 min to homogenize the temperature distribution, and then continuously compressed up to a height reduction of 50%, followed by quenching.

The microstructure and orientation imaging microscopy (OIM) images of the specimens before and after the hot compression were characterized by

a field-emission (FE) SEM system (TESCAN MIRA3) equipped with the Oxford EBSD system (AZtec Nordlys Max3) and the EDS (AZtec X-MaxN80) system. Post-mortem on all the deformed specimens was conducted through the FE-SEM system Sirion 200. The SEM specimens were polished up to 0.05 μm with silica suspension, and the EBSD specimens were prepared by mechanical polishing followed by tri-ion beam cutting.

3 Results and discussion

3.1 Initial microstructure

Figure 1 shows the initial microstructure observed on the longitudinal section in the as-received material; Figures 1(a) and (b) show the microstructures characterized by SEM with different magnifications, Fig. 1(c) shows the EBSD map colored with the inverse pole figure, and Fig. 1(d) shows the EDS map of the titanium (Ti) element. As shown in Fig. 1(a), the reinforcing particles exhibit an inhomogeneous and banded distribution, which is mainly due to the particles clustering originated from the solidification process [24] and extrusion deformation that makes the clusters dispersed. Figure 1(b) shows that the TiB_2 particles agglomerated at grain boundaries

(GBs) are equiaxed and ultrafine with average size about 500 nm. Our previous study [25] verified that the particles inside grains distribute more uniformly and have size from 100 to 500 nm. The EBSD map shown in Fig. 1(c) demonstrates that the extruded composite exhibits a strong extrusion texture, i.e., most grains are aligned with either the (001) or the (111) crystal axis parallel to the ED. Moreover, grains are significantly elongated along the ED, and small and dispersed TiB_2 particles distribute along the grain bands, as shown in Fig. 1(c), where high angle GBs (with misorientation angle $\theta > 15^\circ$) are depicted with black lines and low angle GBs (with $2^\circ \leq \theta \leq 15^\circ$) with lime green lines. The TiB_2 particle bands along the elongated GBs were further confirmed by the EDS map shown in Fig. 1(d).

3.2 Flow stress

The true stress–true strain curves of the composite deformed at temperatures from 300 to 450 $^\circ\text{C}$ and strain rates from 0.001 to 1 s^{-1} are shown in Fig. 2. The composite flow behavior, as anticipated, is significantly sensitive to both temperature and strain rate. For all the deformation conditions, the flow stress is characterized by an initial rapid increase to the peak value and a subsequent decrease to the stable stress. The rapid increase of the flow stress is due to the dislocations

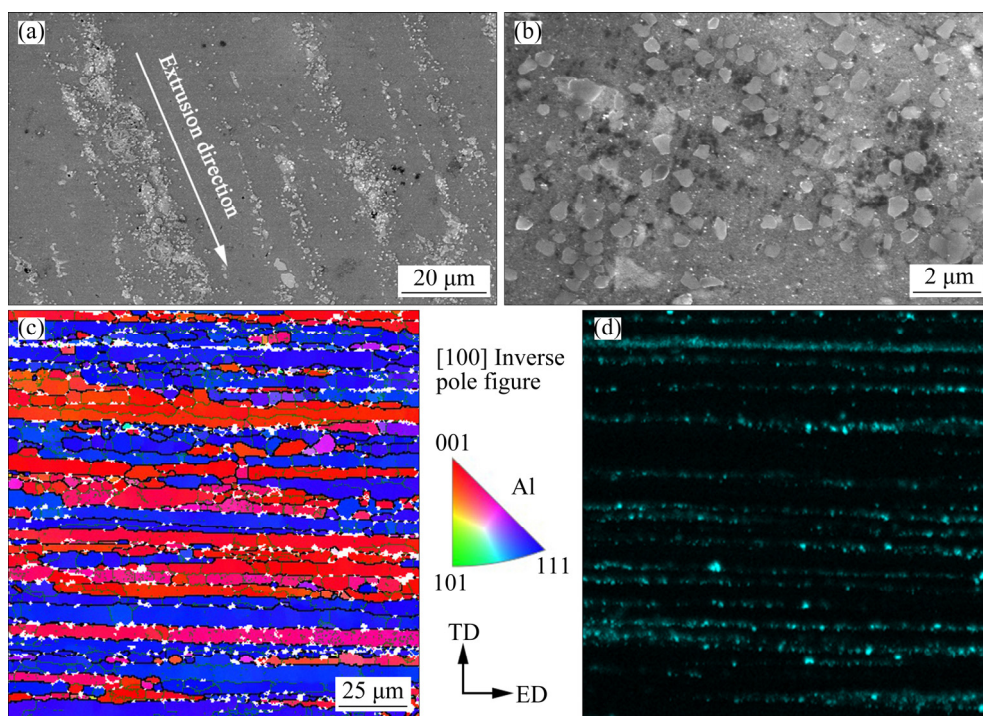


Fig. 1 SEM images of in-situ $\text{TiB}_2/7075\text{Al}$ composite (a, b), EBSD map showing grain structure of composite (c) and EDS map of titanium (Ti) element distribution (d)

pinning by the nanoparticles; while the stress saturation is due to the balance between work hardening and dynamic recovery and DRX [26].

Figure 3(a) presents the variation of the peak stress with respect to strain rate and temperature. The peak stress is quite sensitive to both strain rate and temperature. The maximal peak stress is about

140 MPa in the case of $T=300\text{ }^{\circ}\text{C}$ and $\dot{\epsilon}=1\text{ s}^{-1}$, and the minimum peak stress is less than 12 MPa in the case of $T=450\text{ }^{\circ}\text{C}$ and $\dot{\epsilon}=0.001\text{ s}^{-1}$. Figure 3(b) presents the variation of the strain rate sensitivity m with respect to strain rate under different temperatures, and it is shown that m increases with the increase of temperature. At the deformation

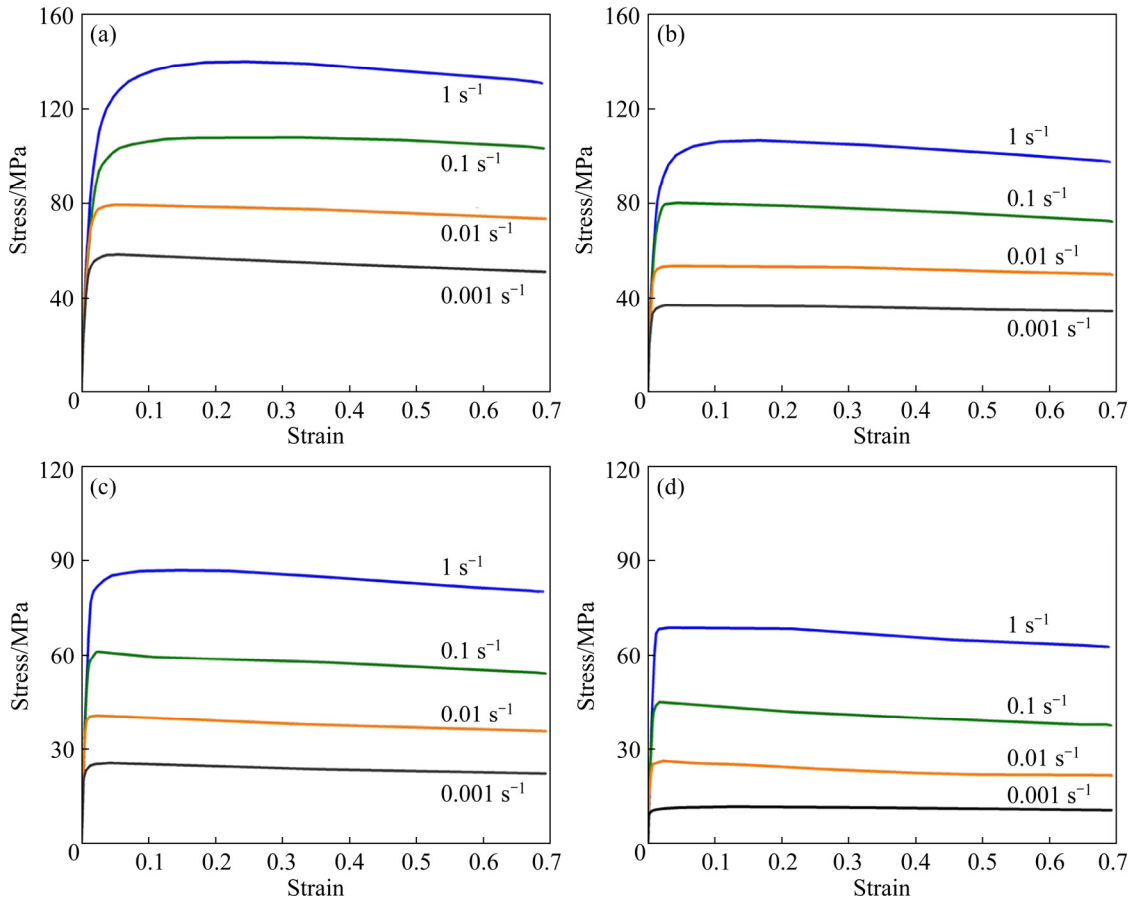


Fig. 2 Hot compression stress–strain curves of in-situ $\text{TiB}_2/7075\text{Al}$ composite in temperature range of 300–450 °C and strain rate range of 0.001–1 s^{-1} : (a) 300 °C; (b) 350 °C; (c) 400 °C; (d) 450 °C

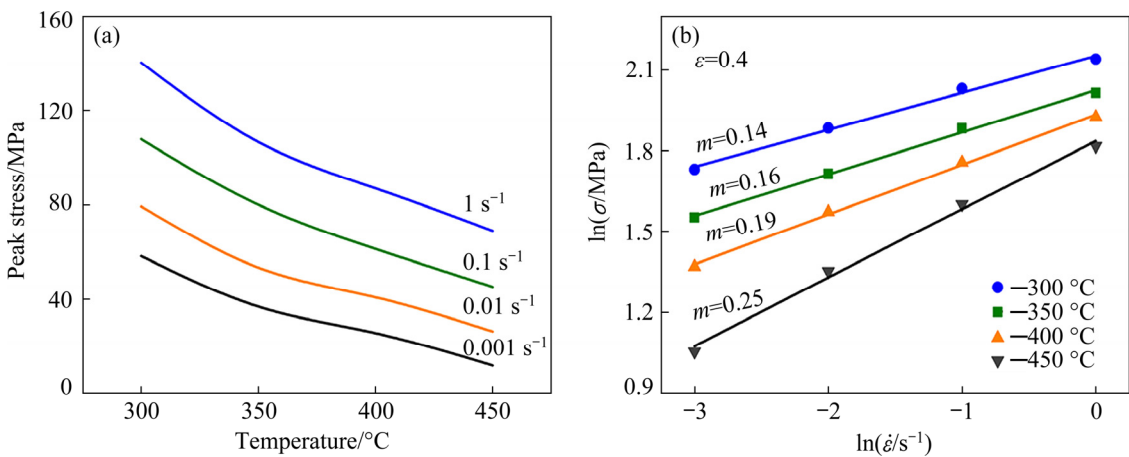


Fig. 3 Evolution of peak stress as function of temperature for strain rates of 1, 0.1, 0.01 and 0.001 s^{-1} (a) and $\lg \sigma\text{--}\lg \dot{\epsilon}$ curves for in-situ $\text{TiB}_2/7075\text{Al}$ composite at true strain of 0.4 (b)

temperature of 450 °C, m has the maximum value of 0.25.

3.3 Constitutive analysis

Establishing the constitutive model related to the strain rate and temperature of the material plastic flow is an essential way to understand the hot deformation behavior of metals and alloys. ZENER and HOLLOMON proposed a temperature-compensated strain rate factor, i.e., the Z parameter, to describe the influence of deformation temperature and strain rate on the flow stress of materials, which is written as

$$Z = \dot{\epsilon} \exp\left(\frac{Q}{RT}\right) \quad (1)$$

where $\dot{\epsilon}$ is the strain rate (s^{-1}), R is the gas constant ($8.3145 \text{ J}/(\text{mol}\cdot\text{K})$), Q is the activation energy of hot deformation (J/mol), and T is the temperature (K). The relationship between Z parameter and flow stress under hot deformation is popularly formulated as the Arrhenius-type equation:

$$Z = \dot{\epsilon} \exp\left(\frac{Q}{RT}\right) = A[\sinh(\alpha\sigma)]^n, \text{ for all } \sigma \quad (2)$$

and can be simplified as

$$Z = \dot{\epsilon} \exp\left(\frac{Q}{RT}\right) = A\sigma^{n_1}, \alpha\sigma < 0.8 \quad (3)$$

$$Z = \dot{\epsilon} \exp\left(\frac{Q}{RT}\right) = A\exp(\beta\sigma), \alpha\sigma < 1.2 \quad (4)$$

where σ is the flow stress (MPa), A is the material factor, $\alpha(=\beta/n_1)$ is the stress multiplier (mm^2/N), and n_1 and n are material constants at a given strain.

The material parameters used in Eq. (2) can be determined at a given strain, and be regressed as a function of strain. For example, when the strain is 0.4, Fig. 4(a) shows the relationships between $\ln \sigma$ and $\ln \dot{\epsilon}$ at different temperatures; the parameter n_1 , obtained from the average slope of these lines, is ~ 5.74 . Figure 4(b) shows the relationships between σ and $\ln \dot{\epsilon}$ at different temperatures; the parameter β , obtained from the average slope of these lines, is 0.104. Then, α is 0.018. The activation energy Q at a given strain rate can be obtained by taking the

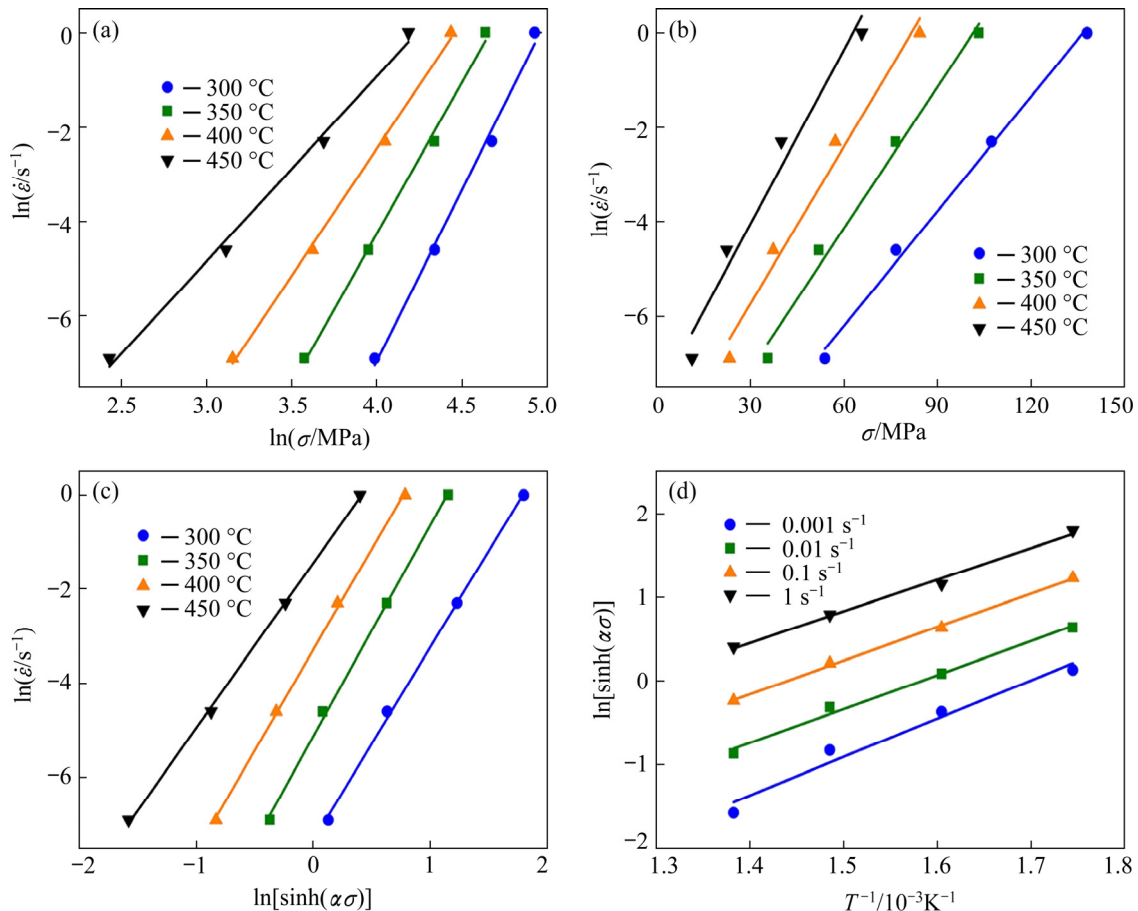


Fig. 4 Relationships between strain rate and flow stress at true strain of 0.4 for in-situ $\text{TiB}_2/7075\text{Al}$ composite: (a) $\ln \dot{\epsilon} - \ln \sigma$; (b) $\ln \dot{\epsilon} - \sigma$; (c) $\ln \dot{\epsilon} - \ln[\sinh(\alpha\sigma)]$; (d) $\ln[\sinh(\alpha\sigma)] - 1000/T$

logarithm of both sides of Eq. (2), which yields

$$Q = Rn \frac{d\{\ln[\sinh(\alpha\sigma)]\}}{d(1000/T)} = Rnk \quad (5)$$

where n and k are respectively the slopes of the $\ln \dot{\epsilon} - \ln[\sinh(\alpha\sigma)]$ and $\ln[\sinh(\alpha\sigma)] - 1000/T$ plots, as shown in Figs. 4(c) and (d), respectively. The mean values of n and k are calculated to be 4.10 and 4.11, respectively. The activation energy Q is found to be 139.97 kJ/mol, which is similar to that for the lattice self-diffusion activation energy of aluminum (144 kJ/mol).

Using the procedures introduced above, the four parameters α , n , Q and $\ln A$ are evaluated for strain values of 0.1–0.6 in steps of 0.05, and regressed as the function of strain, as shown in Fig. 5, where the correlation coefficient is >98%. Therefore, by considering temperature, strain and strain rate conditions, the flow stress of the in-situ TiB₂/7075Al composite during hot deformation can be predicted by the following constitutive equation:

$$\sigma = \frac{1}{\alpha} \ln \left\{ \left(\frac{Z}{A} \right)^{1/n} + \left[\left(\frac{Z}{A} \right)^{2/n} + 1 \right]^{1/2} \right\} \quad (6)$$

3.4 Fractographs and microstructure evolution

In the hot deformation of PR-ALMCs, the flow behavior was mainly governed by two processes, i.e., the transfer of stress from the ductile matrix to the hard particles and the microstructure evolution including recrystallization and damage evolution [27]. Because of different deformation behaviors of the particles and the matrix, the plastic deformation of the composite is intrinsically inhomogeneous, and dislocations are significantly hindered by the particles, which results in the stress concentration. Figure 6 shows the SEM images of the deformed specimens under conditions of 300 °C, 1 s⁻¹; 300 °C, 0.1 s⁻¹; and 350 °C, 0.01 s⁻¹. As shown in Figs. 6(a) and (c), plenty of particle cracks can be found under conditions of $T=300$ °C, $\dot{\epsilon}=1$ s⁻¹ and $T=300$ °C, $\dot{\epsilon}=0.1$ s⁻¹, respectively. Severe interface debonding and crack propagation

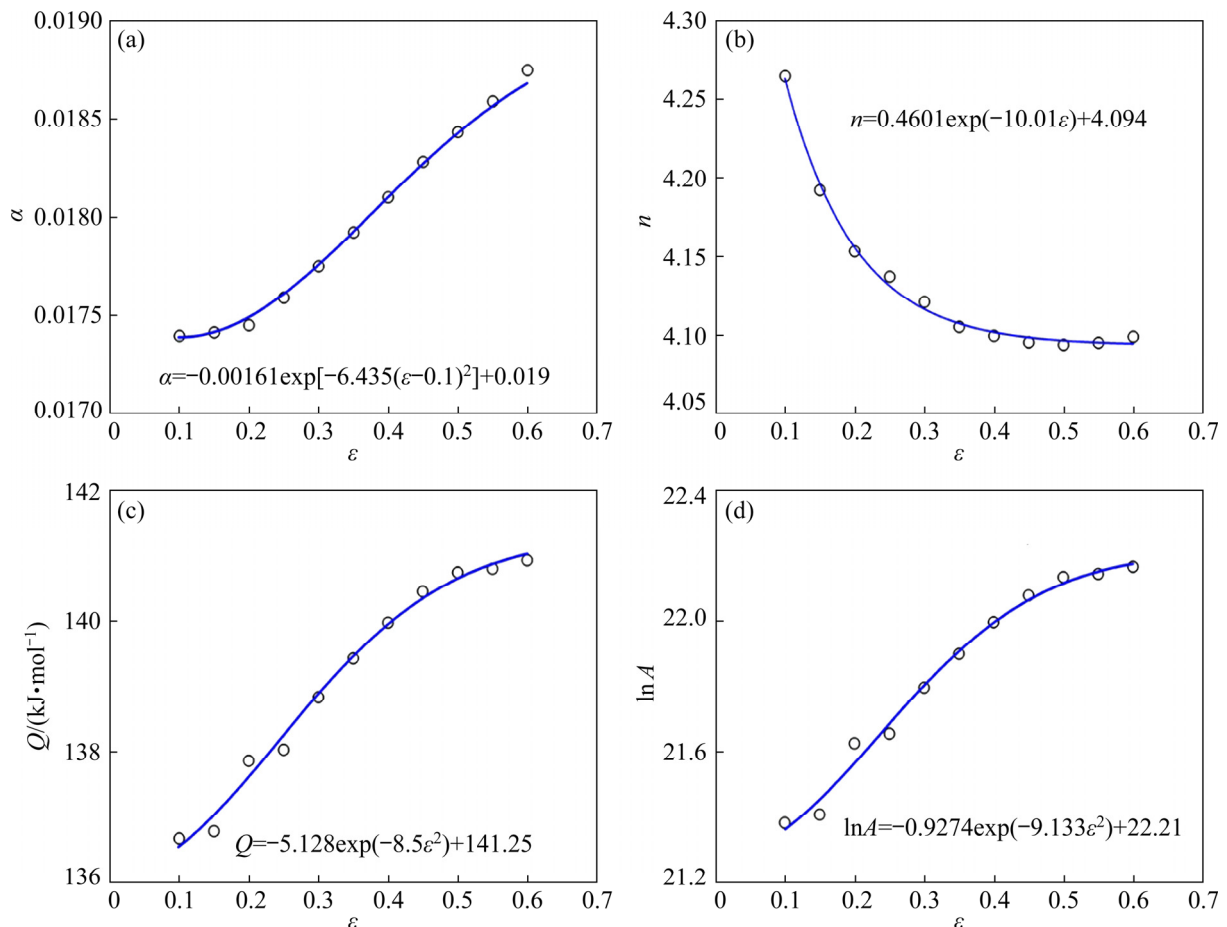


Fig. 5 Fitting curves of material constants with true strain (ϵ): (a) α ; (b) n ; (c) Q ; (d) $\ln A$

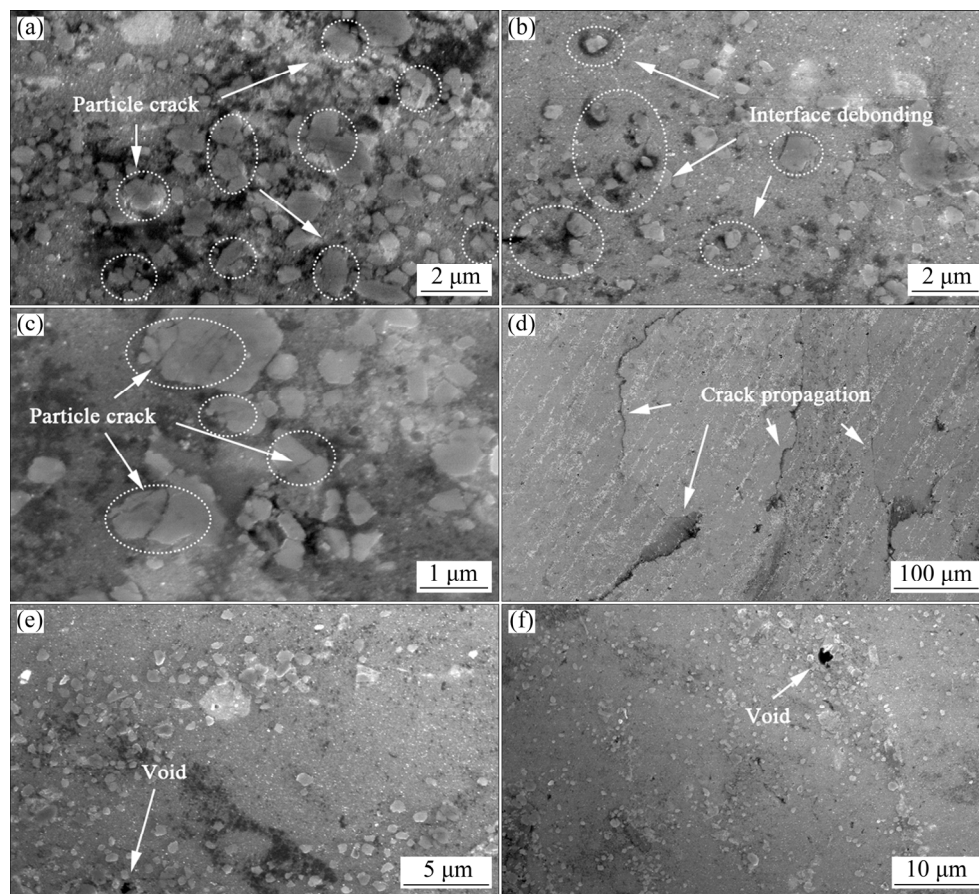


Fig. 6 SEM images with different magnifications for in-situ $\text{TiB}_2/7075\text{Al}$ composite after hot deformation under different conditions: (a, b) $300\text{ }^\circ\text{C}$, 1 s^{-1} ; (c, d) $300\text{ }^\circ\text{C}$, 0.1 s^{-1} ; (e, f) $350\text{ }^\circ\text{C}$, 0.01 s^{-1}

can be found in Figs. 6(b) and (d), respectively, which indicates that these two conditions are not suitable for the hot forming of this composite. From Figs. 6(a) to (d), one can see that larger irregular particles are more inclined to fracture than smaller equiaxial particles. Similar phenomenon was also reported by YAN et al [28] and ROMANOVA et al [29] for PR-ALMCs. Under deformation conditions of $T=350\text{ }^\circ\text{C}$ and $\dot{\epsilon}=0.01\text{ s}^{-1}$, as shown in Figs. 6(e) and (f), only a few voids are observed. As the temperature increases, both particle crack and interface debonding are not observed. This is attributed to the decreased strength of the matrix at high temperature and the subsequent lowered stress at the particle/matrix interfaces, which decreases the possibility of particle crack or interface debonding [15].

Figure 7 shows the SEM images of the deformed specimens under conditions of $T=400\text{ }^\circ\text{C}$ and $450\text{ }^\circ\text{C}$ with 0.001 and 0.1 s^{-1} . Voids can be clearly seen in all the specimens while particle crack is scarcely observed. With the increase of

temperature or the decrease of strain rate, the matrix becomes softer and easier to accommodate the particles. This is because at high temperature dislocations have more opportunity to bypass the impenetrable obstacles by the thermally activated mechanism or even by a climbing mechanism. Thus, the heterogeneous deformation resulted from the existence of particles can be relieved, so that the local concentrated stress is not high enough to break up the particles. However, the deformability difference between the particles and the matrix is still significant even at high temperatures. As a result, the heterogeneous deformation is released by means of void nucleation and growth instead of particle crack.

In order to study the microstructure evolution of the in-situ $\text{TiB}_2/7075\text{Al}$ composite after hot deformation, EBSD characterization was performed on the deformed specimens. Figure 8 shows the EBSD maps and corresponding grain size distribution of the composite after the hot deformation under different testing conditions

(300 °C, 0.001 s⁻¹; 450 °C, 1 s⁻¹; 450 °C, 0.001 s⁻¹). The microstructure and grain size distribution of the composite deformed at 300 °C, 0.001 s⁻¹ are shown in Figs. 8(a) and (d). Plenty of fine DRX grains and some inherited coarse grains can be seen in Fig. 8(a), which implies the occurrence of partial DRX. The coarse grains have the size similar to those of the as-received composite (22–43 μm), and the size of the fine grains is in the range of 0.5–10 μm. For this hot deformation

condition, the DRX fraction is about 35% according to the area fraction of the fine grains. The microstructure and grain size distribution of the composite deformed at 450 °C and 1 s⁻¹ are shown in Figs. 8(b) and (e), respectively, which also exhibit the typical partial DRX phenomenon similar to the condition above. The size of the coarse grains is 15–35 μm, the size of the fine grains is 0.5–10 μm, and the DRX fraction is computed to be about 60%. As shown in Figs. 8(c) and (f), the

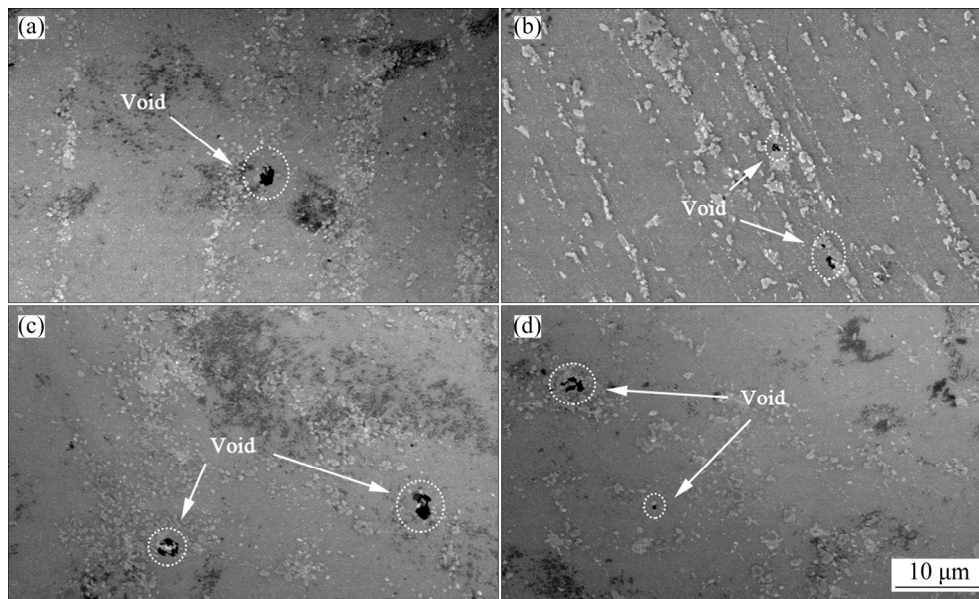


Fig. 7 SEM images of in-situ TiB₂/7075Al composite after hot deformation under different testing conditions: (a) 400 °C, 0.1 s⁻¹; (b) 400 °C, 0.001 s⁻¹; (c) 450 °C, 0.1 s⁻¹; (d) 450 °C, 0.001 s⁻¹

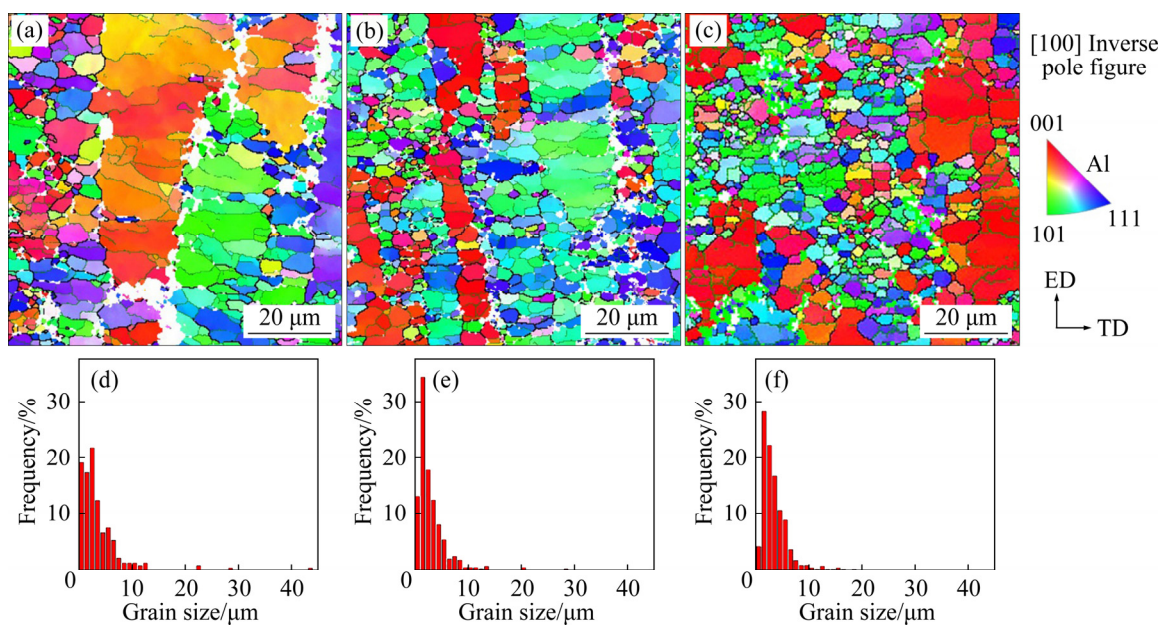


Fig. 8 EBSD maps showing microstructures of in-situ TiB₂/7075Al composite after hot deformation (a–c) and statistical grain size distribution of deformed specimens (d–f) under different testing conditions: (a, d) 300 °C, 0.001 s⁻¹; (b, e) 450 °C, 1 s⁻¹; (c, f) 450 °C, 0.001 s⁻¹

specimen deformed 450 °C and 0.001 s⁻¹ shows a homogeneous microstructure with a uniform and fine grain size distribution. Besides, the DRX fraction is about 85% and the DRX grains have an average aspect ratio about 0.8 and average size about 2.5 μm, which is much smaller than the grain size of the as-received composite.

Compared with the 7075Al alloy (sizes of 15–20 μm [30,31]) or the ex-situ 7075Al matrix composite (about 50 μm [32]) after the similar hot compression deformation treatment, the studied in-situ TiB₂/7075Al composite has finer grain size. This is mainly attributed to the ultrafine in-situ particles in the composite, which are able to effectively pin the mobile dislocations, promote the DRX nucleation, and inhibit the grain growth by pinning the migration of GBs, thus resulting in the uniform and fine DRX grain structure [33–35]. Figure 9 shows the schematic diagrams of interactions of the dislocation–particles and the GB–particles. During the deformation, the in-situ particles, in comparison with the traditional ex-situ particles, can effectively relieve the stress rising caused by dislocation accumulation at the interfaces. The local stress shared by each particle is more

compatible, and the particle thus has a better tolerance to fracture. By contrast, the particles in the ex-situ composite are more prone to fracture for their large size and irregular shape that result in the stress concentration. As shown in Figs. 9(c) and (d), under the condition of high temperature deformation, the uniform distribution of in-situ particles leads to more nucleation points of DRX. During grain growth, GB is easily hindered by in-situ particles. Therefore, the recrystallization grain size of in-situ TiB₂/7075Al composite is smaller than that of ex-situ composite.

3.5 Processing maps

According to the previous SEM and EBSD analysis on the fracture mechanisms and microstructure evolution of the composite, herein processing maps (PMs) were further employed to quantify the formability and the failure of the composite under different deformation conditions. PMs can be used to evaluate the material formability as a function of process parameters such as temperature, strain rate, and strain levels [36,37]. The stability zone prescribes the process condition suitable for hot forming and the instability zone

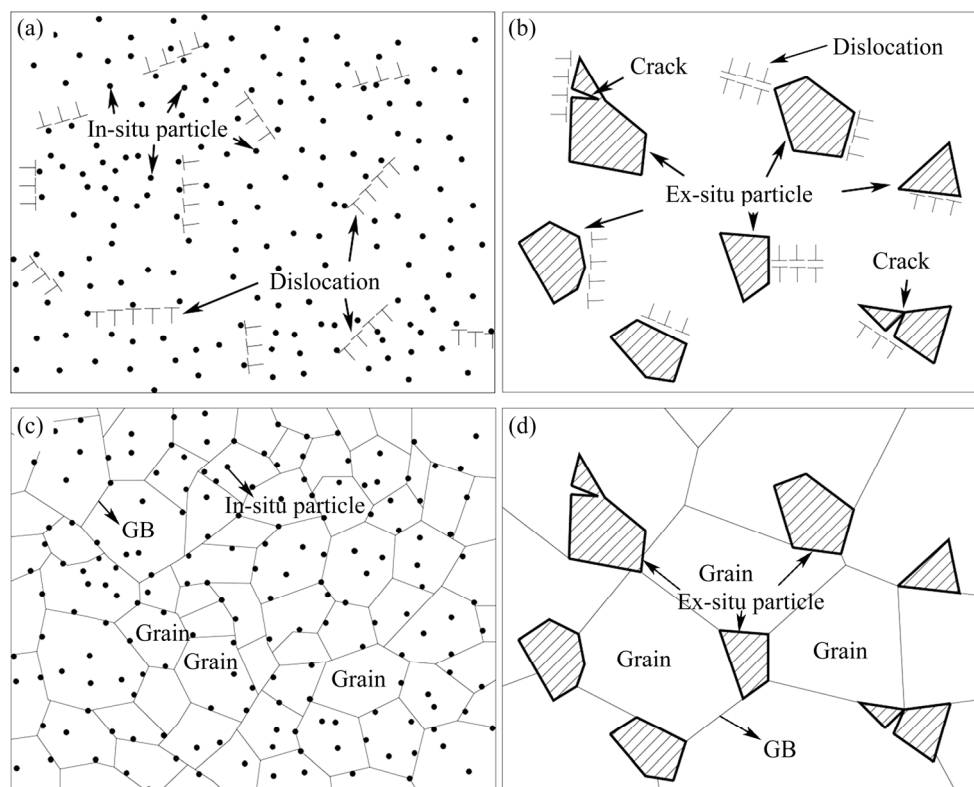


Fig. 9 Schematic diagrams showing interactions of dislocation–particles and GB–particles: (a) Dislocations pinned by in-situ particles; (b) Dislocations pinned by ex-situ particles; (c) GBs pinned by in-situ particles; (d) GBs pinned by ex-situ particles

prescribes process condition unsuitable for hot forming. In particular, the PM based on the dynamic material model (DMM) proposed by PRASAD [38] is widely used; it considers the work-piece as a power dissipator during the deformation. MURTY and RAO [39] modified the DMM and proposed a stricter description of power dissipation by considering microstructure evolution, namely, the MDMM. For describing the flow instability, there are two types of instability criteria: one is derived from Ziegler’s plastic flow theory, including the Prasad’s instability criterion and the Murty’s criterion, and the other is derived from the Lyapunov’s functions, including the Gegel’s instability criterion and the Malas’s criterion. In this study, three widely used instability criteria, i.e., the Prasad’s, Murty’s, and Gegel’s criteria, were considered to construct the PMs of the composite [40].

Figures 10(a) and (b) show the power dissipation maps (PDMs) of the in-situ TiB₂/7075Al composite in the entire temperature and strain rate ranges considered. The values on the contour lines represent the specific power dissipation efficiency (PDE, η), and the regions with peak η values

indicate the optimal process conditions (a high PDE value is usually associated with dynamic recovery, DRX, and superplasticity) [41]. Both PDMs obtained from the DMM and MDMM have two domains with peak efficiencies. The first domain is in the temperature range of 300–350 °C and the strain rate range of 0.005–0.05 s⁻¹, and the peak efficiency is 28% when $T=330$ °C and $\dot{\epsilon}=0.01$ s⁻¹. The second one is in the temperature range of 425–450 °C and the strain rate range of 0.001–0.02 s⁻¹, and the peak efficiency is 46% when $T=450$ °C and $\dot{\epsilon}=0.001$ s⁻¹. As a result, the second domain with the higher peak efficiency is more suitable for hot working under the test conditions, especially in the temperature range of 425–450 °C and the strain rate range of 0.001–0.01 s⁻¹. Figures 10(c) and (d) show the strain rate sensitivity (m) map and temperature sensitivity (s) map, respectively. The region with the highest m and the highest s correspond to the region of maximum ductility. A higher m indicates a smaller possibility of damage, and a larger s represents more sufficient dynamic softening and better formability [42]. As shown in Fig. 10(c), there are two domains with peak value of m , which is similar to the PDMs. As

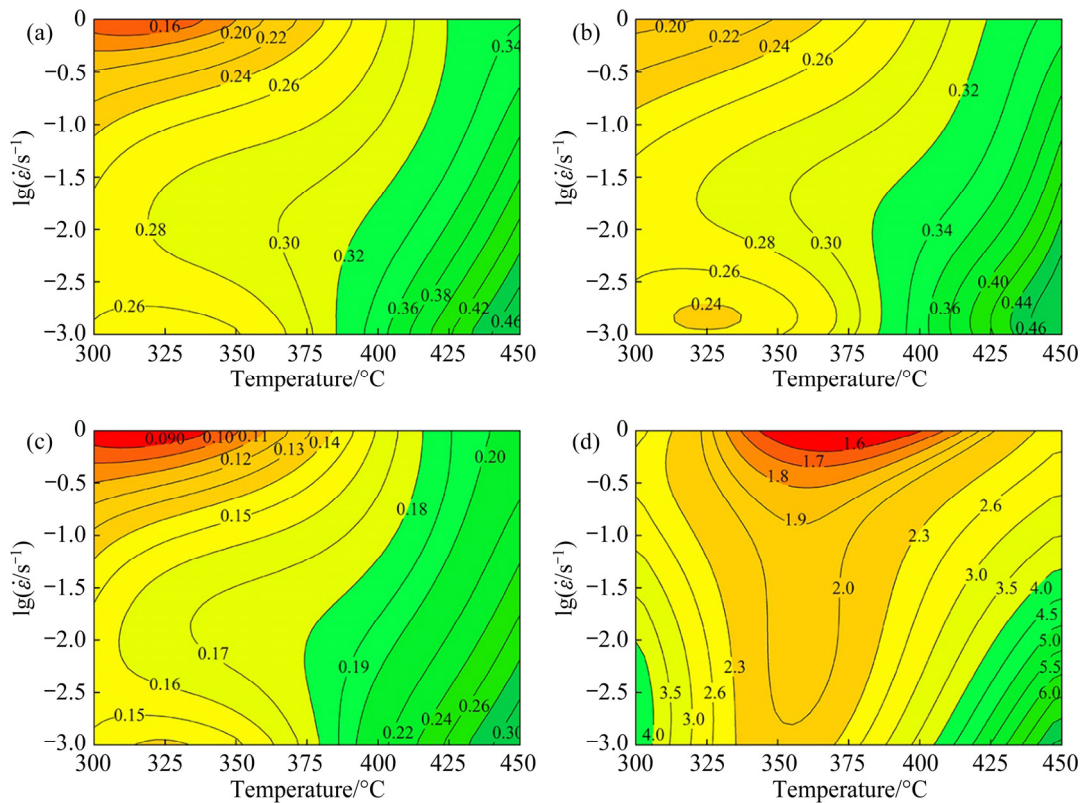


Fig. 10 PDMs (η) based on DMM (a) and MDMM (b), strain rate sensitivity (m) map (c), and temperature sensitivity (s) map (d) of in-situ TiB₂/7075Al composite at true strain of 0.4

shown in Fig. 10(d), the map of s exhibits two main peak domains at a low strain rate. The first domain is located in the temperature range of 300–325 °C and the strain rate range of 0.001–0.01 s⁻¹, and the second domain is located in the temperature range of 425–450 °C and the strain rate range of 0.001–0.01 s⁻¹. This phenomenon indicates that these two domains at low strain rates are in more favor of hot deformation. The temperature in the domains with peak efficiencies of the in-situ TiB₂/7075Al composite is similar to that of 7075Al (400–460 °C), but the strain rate is lower than that of 7075Al (for 7075Al, it is 0.1–0.01 s⁻¹) [31]. This is due to the pinning effect of the particles on the dislocation, and enough dislocation density can be accumulated to produce dynamic recovery and DRX at lower strain rates.

Figures 11(a–c) show the PMs with different instability criteria at a true strain of 0.4, and the red shaded domains represent the instability regions. The instability region obtained by the Prasad's criterion dominates in the temperature range of 300–400 °C and the strain rate range of 0.03–1 s⁻¹,

and the region obtained by the Murty's criterion dominates in the temperature range of 300–375 °C and the strain rate range of 0.3–1 s⁻¹. Although both the Prasad's and Murty's instability regions locate at low temperatures and high strain rates, the first one is obviously larger than the second one. Notably, as shown in Fig. 11(c), the flow instability region obtained by the Gegel's criterion is significantly different from the former two. The Gegel's instability map exhibits two main flow instability regions at low temperatures, one at high strain rate and the other at low strain rate. The region at low temperatures and low strain rates (325–375 °C and 0.003–0.03 s⁻¹) shows a relatively high PDE, which is also within the Gegel's instability region.

Combining the microscopic observations in Section 3.4 and the predicted instability regions above, it is concluded that both the Murty's and the Gegel's criteria predict smaller instability regions than the actual one. By contrast, the Prasad's criterion is more appropriate for the composite deformed under conditions of low temperature and

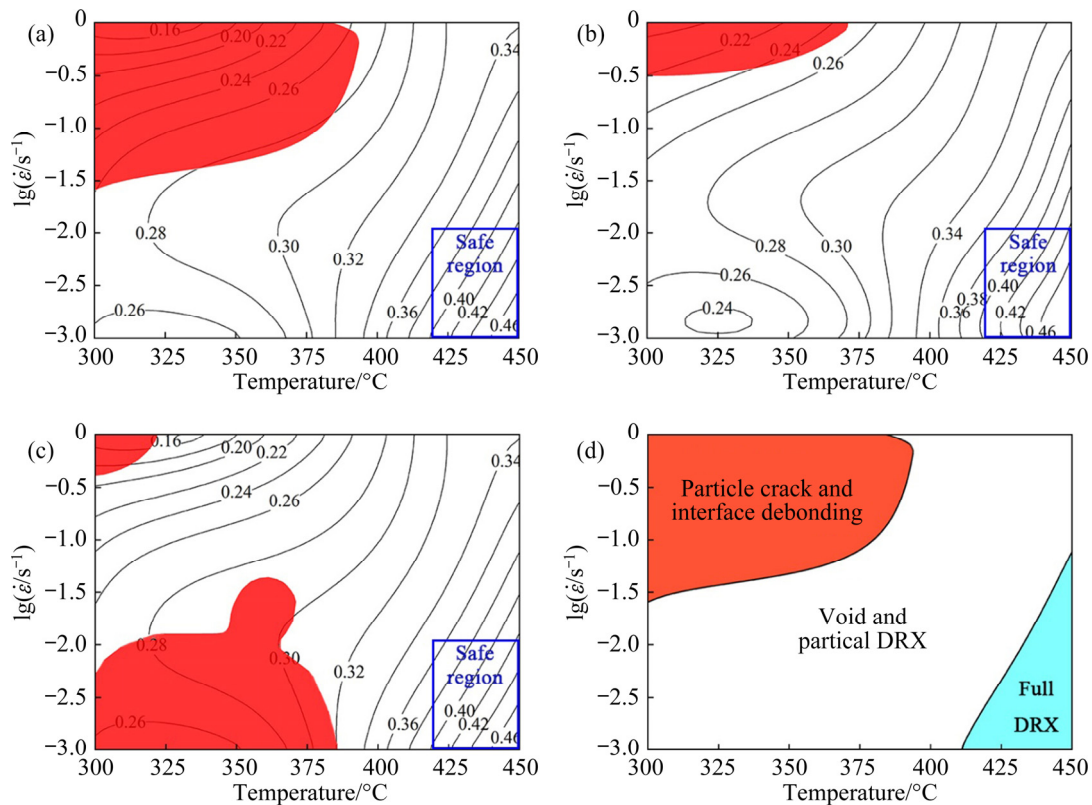


Fig. 11 PMs based on three different instability criteria and microstructure evolution mechanism schematic diagram of in-situ TiB₂/7075Al composite at true strain of 0.4: (a) DMM and Prasad's instability criterion; (b) MDM and Murty's instability criterion; (c) DMM and Gegel's instability criterion; (d) Schematic diagram for microstructure evolution mechanism of composite under different testing conditions

low strain rate. For the deformation conditions of $T=350\text{ }^{\circ}\text{C}$ and $\dot{\epsilon}=0.01\text{ s}^{-1}$, which are within the Gegel's flow instability region, no micro-crack is observed in the deformed specimen, as shown in Figs. 6(e) and (f). Hence, the instability domains predicted by the Gegel's criterion are not reasonable.

As stated previously, the composite failed mainly by two modes, i.e., particle crack and interface debonding. Synthesizing these microscopic observations and the PMs above, the microstructure evolution mechanisms of the $\text{TiB}_2/7075\text{Al}$ composite under different testing conditions are schematically illustrated in Fig. 11(d). The instability domain is located in the conditions of low temperatures and high strain rates, and the PDE in this domain is less than 28%. In the stability regions, the SEM image of the deformed composite shows very few voids. In the middle region of the PM, the PDE is 28%–38%, which is higher than the typical value of dynamic recovery (15%–25%), but lower than that of DRX (35%–50%). This indicates that the mechanism of microstructure evolution in this domain is controlled by both partial DRX and dynamic recovery. Under the conditions of high temperature and low strain rate, full DRX renders a uniform and fine grain size. Generally, the DRX domain is suggested for hot deformation of the studied composite because it not only provides high PDE (more than 38%), stable flow, and good formability, but also renders desired microstructures.

4 Conclusions

(1) Under deformation conditions of low temperatures (300–375 °C) and high strain rates (0.03–1 s⁻¹), the main damage mechanisms of the in-situ $\text{TiB}_2/7075\text{Al}$ composite are particle crack and interface debonding. At high temperatures and low strain rates, the heterogeneous deformation is released by means of void nucleation and growth instead of particle crack.

(2) Full DRX occurs at high temperature (450 °C) and low strain rate (0.001 s⁻¹), which refines the grains and further improves the hot formability of the in-situ $\text{TiB}_2/7075\text{Al}$ composite. The grain size of the in-situ $\text{TiB}_2/7075\text{Al}$ composite is obviously smaller than that of the 7075Al alloy and the ex-situ 7075Al matrix composite. This is

attributed to the promotion of nucleation and inhibition of grain growth by the fine in-situ particles with uniform dispersion.

(3) Both the PMs based on DMM and MDMM are reliable to predict the stability domain. The Prasad's instability criterion can be used to predict an accurate instability region, and the Murty's prediction is smaller than the actual one.

(4) The optimum domain for the hot deformation of the in-situ $\text{TiB}_2/7075\text{Al}$ composite is at the temperature of 425–450 °C and strain rate of 0.001–0.01 s⁻¹. The instability domain is at the temperature of 300–375 °C and strain rate of 0.03–1 s⁻¹.

Acknowledgements

The authors gratefully acknowledge the funding supports from the National Science and Technology Major Project of the Ministry of Science and Technology of China (No. 2018-ZX04044001-008), and the National Natural Science Foundation of China (No. 52075328).

References

- [1] IBRAHIM I A, MOHAMED F A, LAVERNIA E J. Particulate reinforced metal matrix composites—A review [J]. *Journal of Materials Science*, 1991, 26: 1137–1156.
- [2] PRASAD S V, ASTHANA R. Aluminum metal–matrix composites for automotive applications: Tribological considerations [J]. *Tribology Letters*, 2004, 17: 445–453.
- [3] LÜ L, LAI M O, SU Y, TEO H L, FENG C F. In situ TiB_2 reinforced Al alloy composites [J]. *Scripta Materialia*, 2001, 45: 1017–1023.
- [4] MANDAL A, MAITI R, CHAKRABORTY M, MURTY B S. Effect of TiB_2 particles on aging response of Al–4Cu alloy [J]. *Materials Science and Engineering A*, 2004, 386: 296–300.
- [5] CAVALIERE P. Isothermal forging of AA2618 reinforced with 20% of alumina particles [J]. *Composites Part A: Applied Science and Manufacturing*, 2004, 35: 619–629.
- [6] LLOYD D J. Particle reinforced aluminium and magnesium matrix composites [J]. *International Materials Reviews*, 2013, 39: 1–23.
- [7] LUAN Bai-feng, QIU Ri-sheng, LI Chun-hong, YANG Xiao-fang, LI Zhi-qiang, ZHANG Di, LIU Qing. Hot deformation and processing maps of $\text{Al}_2\text{O}_3/\text{Al}$ composites fabricated by flake powder metallurgy [J]. *Transactions of Nonferrous Metals Society of China*, 2015, 25: 1056–1063.
- [8] EZATPOUR H R, SAJJADI S A, SABZEVAR M H, CHAICHI A, EBRAHIMI G R. Processing map and microstructure evaluation of AA6061/ Al_2O_3 nanocomposite at different temperatures [J]. *Transactions of Nonferrous Metals Society of China*, 2017, 27: 1248–1256.

- [9] HAO Shi-ming, XIE Jing-pei, WANG Ai-qin, WANG Wen-yan, LI Ji-wen, SUN Hao-liang. Hot deformation behaviors of 35%SiC_p/2024Al metal matrix composites [J]. Transactions of Nonferrous Metals Society of China, 2014, 24: 2468–2474.
- [10] CHEN Shuang, TENG Jie, LUO Hai-bo, WANG Yu, ZHANG Hui. Hot deformation characteristics and mechanism of PM 8009Al/SiC particle reinforced composites [J]. Materials Science and Engineering A, 2017, 697: 194–202.
- [11] GANGOLU S, GOURAV RAO A, SABIROV I, KASHYAP B P, PRABHU N, DESHMUKH V P. Development of constitutive relationship and processing map for Al–6.65Si–0.44Mg alloy and its composite with B₄C particulates [J]. Materials Science and Engineering A, 2016, 655: 256–264.
- [12] SARAVANAN L, SENTHILVELAN T. Investigations on the hot workability characteristics and deformation mechanisms of aluminium alloy–Al₂O₃ nanocomposite [J]. Materials & Design, 2015, 79: 6–14.
- [13] PATEL A, DAS S, PRASAD B K. Compressive deformation behaviour of Al alloy (2014)–10wt.%SiC_p composite: Effects of strain rates and temperatures [J]. Materials Science and Engineering A, 2011, 530: 225–232.
- [14] DONG Cui-ge, CUI Rui, WANG Ri-chu, PENG Chao-qun, CAI Zhi-yong. Microstructures and mechanical properties of Al 2519 matrix composites reinforced with Ti-coated SiC particles [J]. Transactions of Nonferrous Metals Society of China, 2020, 30: 863–871.
- [15] SRIVASTAVA V C, JINDAL V, UHLENWINKEL V, BAUCKHAGE K. Hot-deformation behaviour of spray-formed 2014Al + SiC_p metal matrix composites [J]. Materials Science and Engineering A, 2008, 477: 86–95.
- [16] LI Yu-li, WANG Wen-xian, ZHOU Jun, CHEN Hong-sheng. Hot deformation behaviors and processing maps of B₄C/Al6061 neutron absorber composites [J]. Materials Characterization, 2017, 124: 107–116.
- [17] CERRI E, SPIGARELLI S, EVANGELISTA E, CAVALIERE P. Hot deformation and processing maps of a particulate-reinforced 6061 + 20% Al₂O₃ composite [J]. Materials Science and Engineering A, 2002, 324: 157–161.
- [18] SPIGARELLI S, CERRI E, CAVALIERE P, EVANGELISTA E. An analysis of hot formability of the 6061 + 20% Al₂O₃ composite by means of different stability criteria [J]. Materials Science and Engineering A, 2002, 327: 144–154.
- [19] RAJAMUTHAMILSELVAN M, RAMANATHAN S. Hot deformation behaviour of 7075 alloy [J]. Journal of Alloys and Compounds, 2011, 509: 948–952.
- [20] RAMANATHAN S, KARTHIKEYAN R, GANASEN G. Development of processing maps for 2124Al/SiC_p composites [J]. Materials Science and Engineering A, 2006, 441: 321–325.
- [21] SENTHILKUMAR V, BALAJI A, NARAYANASAMY R. Analysis of hot deformation behavior of Al 5083–TiC nanocomposite using constitutive and dynamic material models [J]. Materials & Design, 2012, 37: 102–110.
- [22] SHAO J C, XIAO B L, WANG Q Z, MA Z Y, LIU Y, YANG K. Constitutive flow behavior and hot workability of powder metallurgy processed 20vol.%SiC_p/2024Al composite [J]. Materials Science and Engineering A, 2010, 527: 7865–7872.
- [23] XU Wen-chen, JIN Xue-ze, XIONG Wen-deng, ZENG Xiang-qian, SHAN De-bin. Study on hot deformation behavior and workability of squeeze-cast 20vol.%SiC_w/6061Al composites using processing map [J]. Materials Characterization, 2018, 135: 154–166.
- [24] CHEN Z, SUN G A, WU Y, MATHON M H, BORBELY A, CHEN D, JI G, WANG M L, ZHONG S Y, WANG H W. Multi-scale study of microstructure evolution in hot extruded nano-sized TiB₂ particle reinforced aluminum composites [J]. Materials & Design, 2017, 116: 577–590.
- [25] TANG Y, CHEN Z, BORBELY A, JI G, ZHONG S Y, SCHRYVERS D, JI V, WANG H W. Quantitative study of particle size distribution in an in-situ grown Al–TiB₂ composite by synchrotron X-ray diffraction and electron microscopy [J]. Materials Characterization, 2015, 102: 131–136.
- [26] KOCKS U F, MECKING H. Physics and phenomenology of strain hardening: The FCC case [J]. Progress in Materials Science, 2003, 48: 171–273.
- [27] CAVALIERE P, CERRI E, LEO P. Hot deformation and processing maps of a particulate reinforced 2618/Al₂O₃/20_p metal matrix composite [J]. Composites Science and Technology, 2004, 64: 1287–1291.
- [28] YAN Y W, GENG L, LI A B. Experimental and numerical studies of the effect of particle size on the deformation behavior of the metal matrix composites [J]. Materials Science and Engineering A, 2007, 448: 315–325.
- [29] ROMANOVA V A, BALOKHONOV R R, SCHMAUDER S. The influence of the reinforcing particle shape and interface strength on the fracture behavior of a metal matrix composite [J]. Acta Materialia, 2009, 57: 97–107.
- [30] JIA Yan-dong, CAO Fu-yang, GUO Shu, MA Pan, LIU Jing-shun, SUN Jian-fei. Hot deformation behavior of spray-deposited Al–Zn–Mg–Cu alloy [J]. Materials & Design, 2014, 53: 79–85.
- [31] YANG Yong-biao, ZHANG Zhi-min, LI Xu-bin, WANG Qiang, ZHANG Yan-hui. The effects of grain size on the hot deformation and processing map for 7075 aluminum alloy [J]. Materials & Design, 2013, 51: 592–597.
- [32] RAJAMUTHAMILSELVAN M, RAMANATHAN S. Development of processing map for 7075Al/20%SiC_p composite [J]. Journal of Materials Engineering and Performance, 2012, 21: 191–196.
- [33] DAN C Y, CHEN Z, JI G, ZHONG S H, WU Y, BRISSET F, WANG H W, JI V. Microstructure study of cold rolling nanosized in-situ TiB₂ particle reinforced Al composites [J]. Materials & Design, 2017, 130: 357–365.
- [34] LIU Jun, CHEN Zhe, ZHANG Feng-guo, JI Gang, WANG Ming-liang, MA Yu, VINCENT J, ZHONG Sheng-yi, WU Yi, WANG Hao-wei. Simultaneously increasing strength and ductility of nanoparticles reinforced Al composites via accumulative orthogonal extrusion process [J]. Materials Research Letters, 2018, 6: 406–412.
- [35] GUO Sheng-li, LI De-fu, CHEN Dong, WANG Hao-wei. Characterization of deformation stability of in-situ TiB₂/6351 composites during hot compression based on Murty criterion

- [J]. Transactions of Nonferrous Metals Society of China, 2010, 20: 267–275.
- [36] GANESAN G, RAGHUKANDAN K, KARTHIKEYAN R, PAI B C. Development of processing maps for Al 6061/15%SiC_p composite material [J]. Materials Science and Engineering A, 2004, 369: 230–235.
- [37] PRASAD Y V R K, SESHACHARYULU T. Processing maps for hot working of titanium alloys [J]. Materials Science and Engineering A, 1998, 243: 82–88.
- [38] PRASAD Y V R K. Processing maps: A status report [J]. Journal of Materials Engineering and Performance, 2003, 12: 638–645.
- [39] MURTY S V S N, RAO B N. Stability map for hot working of 6061Al–10%vol.% metal matrix composite [J]. Journal of Physics D, 1998, 31: 3306–3311.
- [40] WANG Xiao-hui, LIU Zhen-bao, LUO Hai-wen. Hot deformation characterization of ultrahigh strength stainless steel through processing maps generated using different instability criteria [J]. Materials Characterization, 2017, 131: 480–491.
- [41] KUMAR B K, SAXENA K K, DEY S R, PANCHOLI V, BHATTACHARJEE A. Processing map microstructure evolution correlation of hot compressed near alpha titanium alloy (TiH_y 600) [J]. Journal of Alloys and Compounds, 2017, 691: 906–913.
- [42] WANG Y Z, CAVALIERE P, SPIGARELLI S, EVANGELISTA E. Temperature and strain-rate sensitivity parameters: Analysis of the deformed metal matrix composite A359/SiC/20p [J]. Journal of Materials Science Letters, 2001, 20: 1195–1197.

原位 TiB₂ 颗粒增强 7075 铝基复合材料的热压缩变形行为和显微组织演变

王 涵, 章海明, 崔振山, 陈 哲, 陈 东

上海交通大学 材料科学与工程学院, 上海 200240

摘 要: 采用等温热压缩实验研究不同变形条件下(变形温度 300~450 °C、应变速率 0.001~1 s⁻¹) 原位 TiB₂ 颗粒增强 7075 铝基复合材料的热成形行为、损伤机制和显微组织演变。结果表明, 复合材料在低温和高应变速率下的主要损伤机制是颗粒断裂和界面脱粘, 而在高温和低应变速率下主要是基体的韧窝断裂。此外, 复合材料在高温、低应变速率变形条件下(变形温度 450 °C、应变速率 0.001 s⁻¹)出现完全动态再结晶, 从而提高复合材料的热成形性。热压缩后原位 TiB₂/7075Al 复合材料的晶粒尺寸明显小于 7075Al 和非原位 7075Al 复合材料。根据流动应力实验曲线, 建立原位 TiB₂/7075Al 复合材料包含流变应力、真应变、应变速率和温度的本构方程。基于动态材料模型(DMM)和改进的动态材料模型(MDMM)建立加工图, 分析复合材料的流变失稳区和优化复合材料的热变形工艺参数。复合材料的最佳变形条件为变形温度 425~450 °C、应变速率 0.001~0.01 s⁻¹, 在该变形条件下复合材料的晶粒得到细化, 且不发生颗粒断裂和界面脱粘。

关键词: 原位 TiB₂ 颗粒; 铝基复合材料; 热压缩变形; 颗粒断裂; 界面脱粘; 动态再结晶

(Edited by Wei-ping CHEN)